Supplementary Information

Selective Grafting of Phosphorus onto $Ti_3C_2T_x$ MXene Enables Two-Proton Process and Enhanced Charge Storage

Hao Li[1,7], Ke Fan[1,7], Pei Xiong[1], Hanmo Zhou[1], Zezhou Lin[1], Keyu Tao[2], Tiancheng Liu[1], Xuyun Guo[1], Ye Zhu[1], Lyuchao Zhuang[1], Wei Han[4], Chen Yang[1], Yan Liu[4], Molly Meng-Jung Li[1*], Mingwang Fu[5], John Wang[6], Haitao Huang[1*]

[1]Department of Applied Physics and Research Institute for Smart Energy
The Hong Kong Polytechnic University
Hung Hom, Kowloon, Hong Kong 999077, P. R. China
E-mail: molly.li@polyu.edu.hk (Molly Meng-Jung Li)
aphhuang@polyu.edu.hk (Haitao Huang)

[2]College of Chemistry and Chemical Engineering,
Chongqing University
Shapingba, Chongqing 401331, P. R. China

[3]Hubei Yangtze Memory Laboratories
Wuhan, Hubei, 430205, P. R. China

[4]School of Chemical Engineering and Technology,
Sun Yat-sen University
Tangjiawan, Zhuhai 519082, P. R. China

[5]Department of Mechanical Engineering,
Research Institute for Advanced Manufacturing,
The Hong Kong Polytechnic University
Hung Hom, Kowloon, Hong Kong 999077, P. R. China

[6]Department of Materials Science and Engineering
National University of Singapore
117574, Singapore

[7] These authors contributed equally to this work

Computational details

First-principles calculations were performed in the framework of density functional theory (DFT) implemented in the Vienna ab initio simulation package (VASP).[1, 2] The exchange-correlation functional was described by generalized gradient approximation (GGA) with the Perdew-Burke-Ernzerhof (PBE) flavor.[3, 4] For geometry optimization, the plane-wave cut-off energy was set as 500 eV. The Brillouin zone was sampled using a Monkhorst–Pack *k*-point mesh scheme, and the meshes of Γ-centered 5 × 5 × 1 were used for the 3 × 3 supercell. The convergence criteria for energy and force were set to be 10^{-6} eV and 0.01 eV $Å^{-1}$, respectively. To avoid the interlayer interaction, a vacuum layer was added in *c*-axis with the distance of 16 Å. The charge redistribution and transfer were quantitatively analyzed and estimated by the charge differential analysis and Bader charge method.[5]

The formation energy ΔE of P atoms on $Ti_3C_2O_2$ monolayer was calculated by:

$$\Delta E = E_{Ti_3C_2O_2P_x} - \left(x\mu_P + E_{Ti_3C_2O_2}\right) \quad (1)$$

where $E_{Ti_3C_2O_2P_x}$ and $E_{Ti_3C_2O_2}$ are the total energies of $Ti_3C_2O_2$ with and without P atoms, μ_P represents the energy per P atom in the bulk form and *x* corresponds to the content of phosphorus atoms in the substrate configurations.

The differential charge density was obtained as the difference between the charge density before and after the bonding:[6]

$$\Delta\rho(\vec{r}) = \rho_{Ti_3C_2O_2-P}(\vec{r}) - \rho_P(\vec{r}) - \rho_{Ti_3C_2O_2}(\vec{r}) \quad (2)$$

where $\rho_{Ti_3C_2O_2-P}(\vec{r})$, $\rho_P(\vec{r})$, and $\rho_{Ti_3C_2O_2}(\vec{r})$ represent the charge density distributions of $Ti_3C_2O_2$-P system, P atom, and bare $Ti_3C_2O_2$ monolayer, respectively.

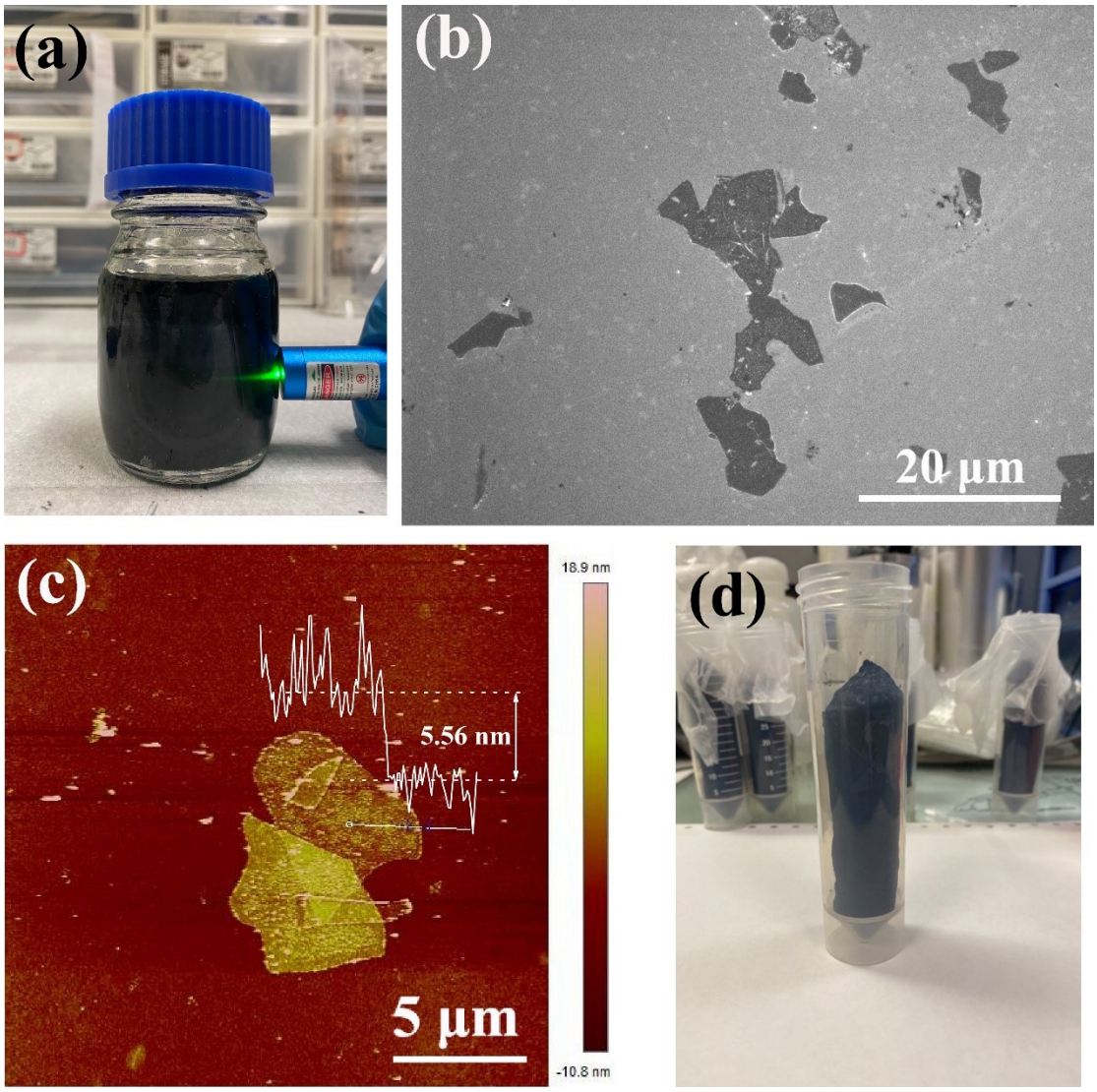

Figure S1 (a) $Ti_3C_2T_x$ MXene colloidal solution shows Tyndall effect. (b) SEM image of $Ti_3C_2T_x$ sheets on silicon substrate. (c) AFM image of $Ti_3C_2T_x$ sheets. Inset shows height profile of the selected line on the upper sheet. (d) Photograph of $Ti_3C_2T_x$ MXene aerogel.

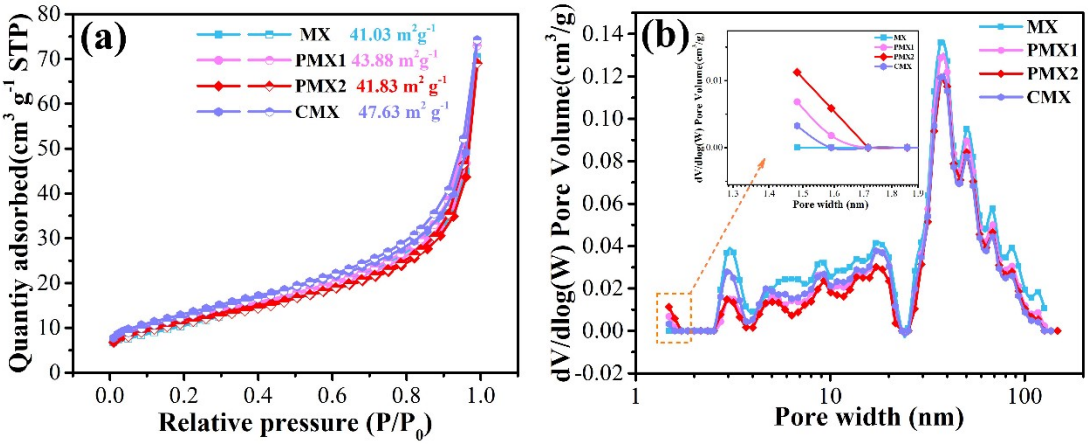

Figure S2 (a) Nitrogen isothermal adsorption/desorption curves and (b) corresponding pore width distribution curves of MX, PMX1, PMX2 and CMX. Inset is the enlarged distribution curve at

small pore width.

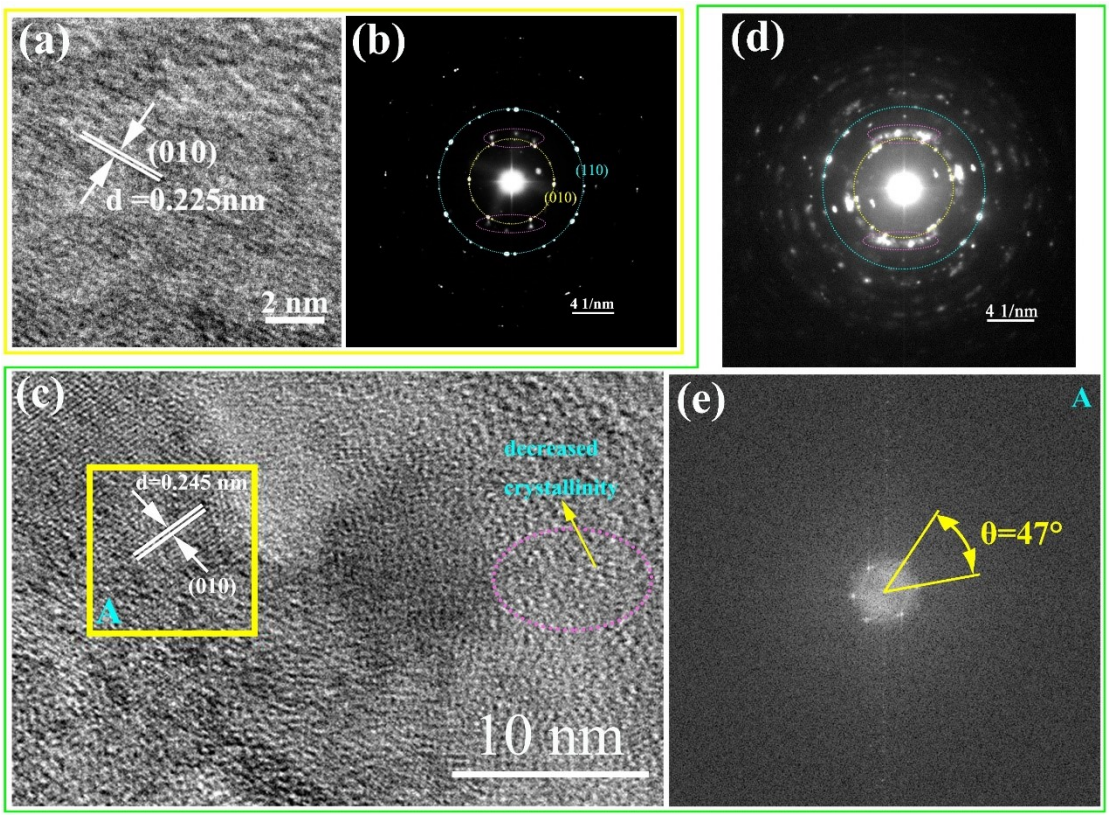

Figure S3 (a) HRTEM image and (b) SAED pattern of PMX8. (c) HRTEM image and (d) SAED pattern of PMX20. (e) FFT pattern of A region in (c).

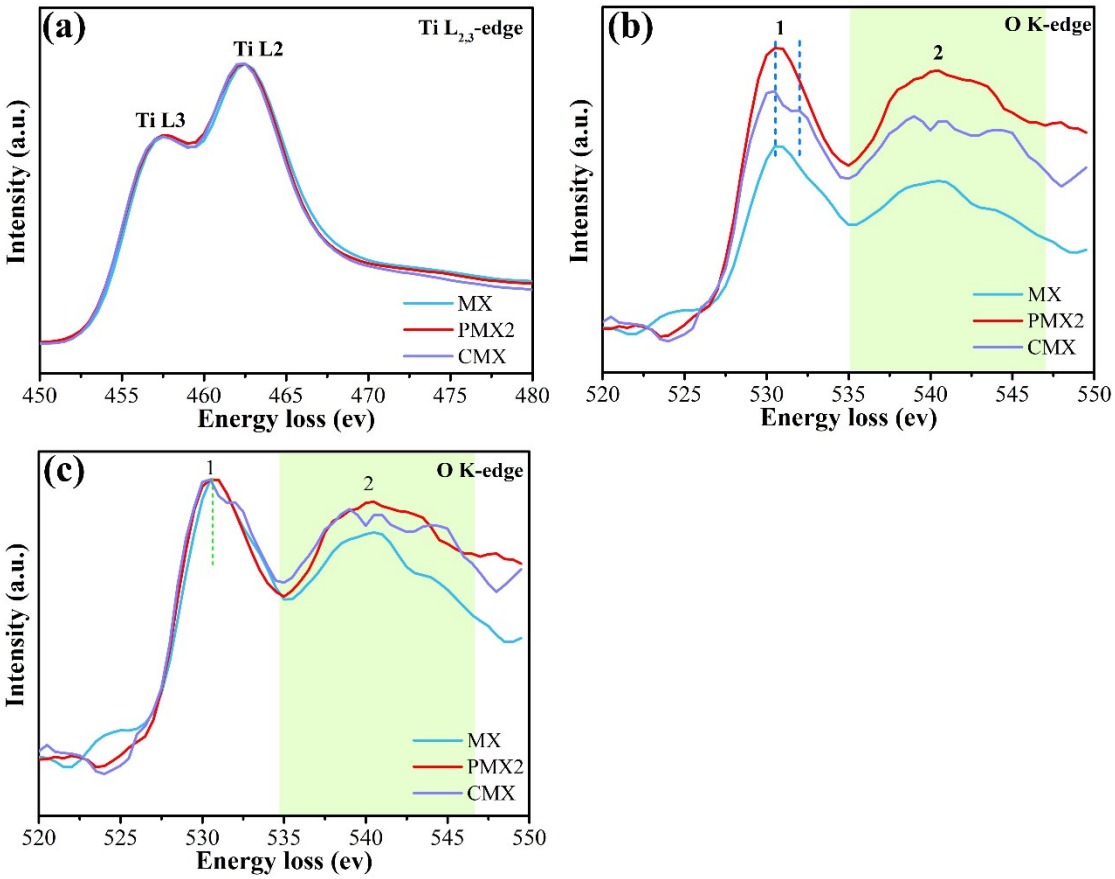

Figure S4 (a) Ti $L_{2,3}$ edge and (b) O K-edge EELS spectra of MX, PMX2 and CMX, in which the EELS intensities of two elements in each sample were normalized to their highest peak values in Ti $L_{2,3}$ edge EELS spectra. (c) O K-edge spectra for the three samples normalized to the first peak intensity (peak 1 in the figure).

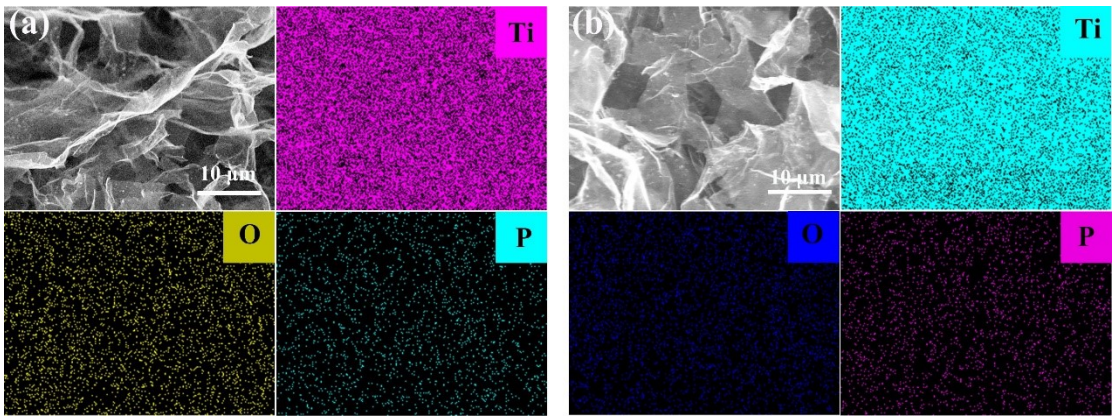

Figure S5 Elemental mapping (Ti, O and P) of (a) PMX1 and (b) PMX2.

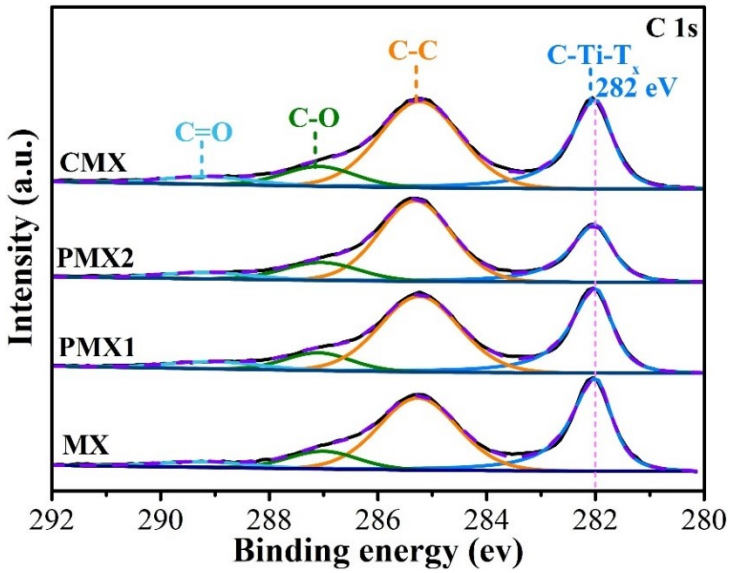

Figure S6 Peak fitting of C1s XPS spectra for MX, PMX1, PMX2 and CMX.

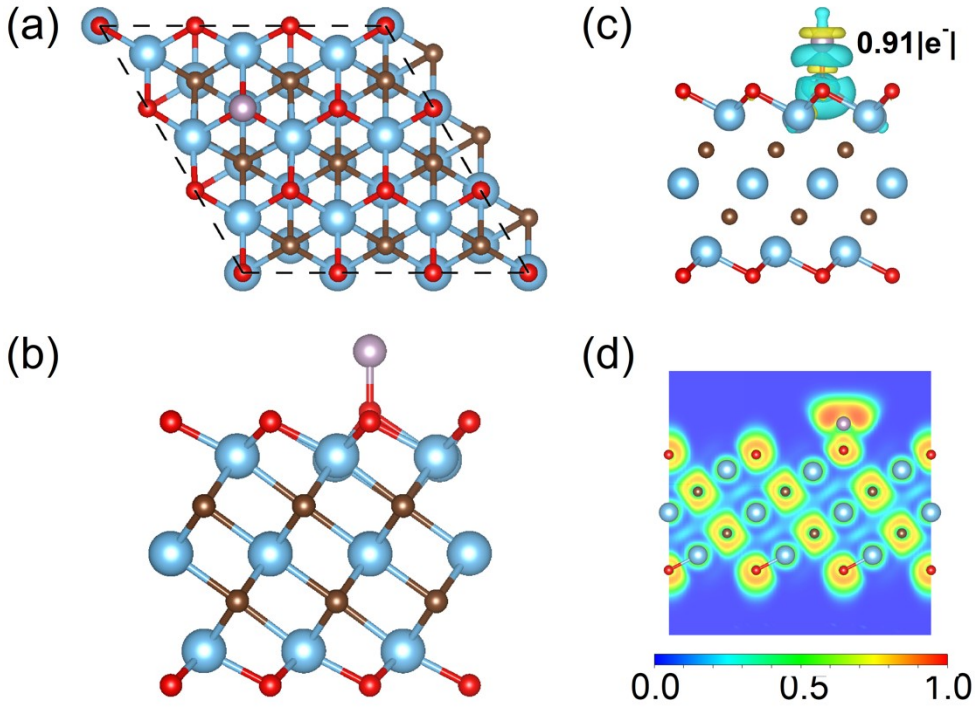

Figure S7. (a) Top and (b) side views of the $Ti_3C_2O_2$-P system; (c) Differential charge density distributions of $Ti_3C_2O_2$-P, yellow and blue regions indicate electron accumulation and depletion, respectively; (d) Electron localization function (ELF) maps of $Ti_3C_2O_2$-P. The scale bar shows the isodensity values of ELF. Ti, C, O, and P atoms are represented in blue, brown, red, and purple, respectively.

Results

This phenomenon has been further proved by DFT calculations. The optimized structure of

$Ti_3C_2O_2$-P system is shown in Figure S7a and b, based on the calculation of formation energy between single P atom and $Ti_3C_2O_2$ substrate, the P atoms can be stably adsorbed above the O atom with a low formation energy of -3.33 eV. Besides, the differential charge density clearly visualizes the charge transfer from the P atom to the $Ti_3C_2O_2$ substrate and mainly to the O atom with the value of 0.91 electron estimated by the Bader charge method (Figure S7c). To better understand the bonding behavior, electron localization function (ELF) has been calculated and the bonds between P–O atoms are covalent in nature (Figure S7d). These results confirm that the bond of P-O can stably exist.

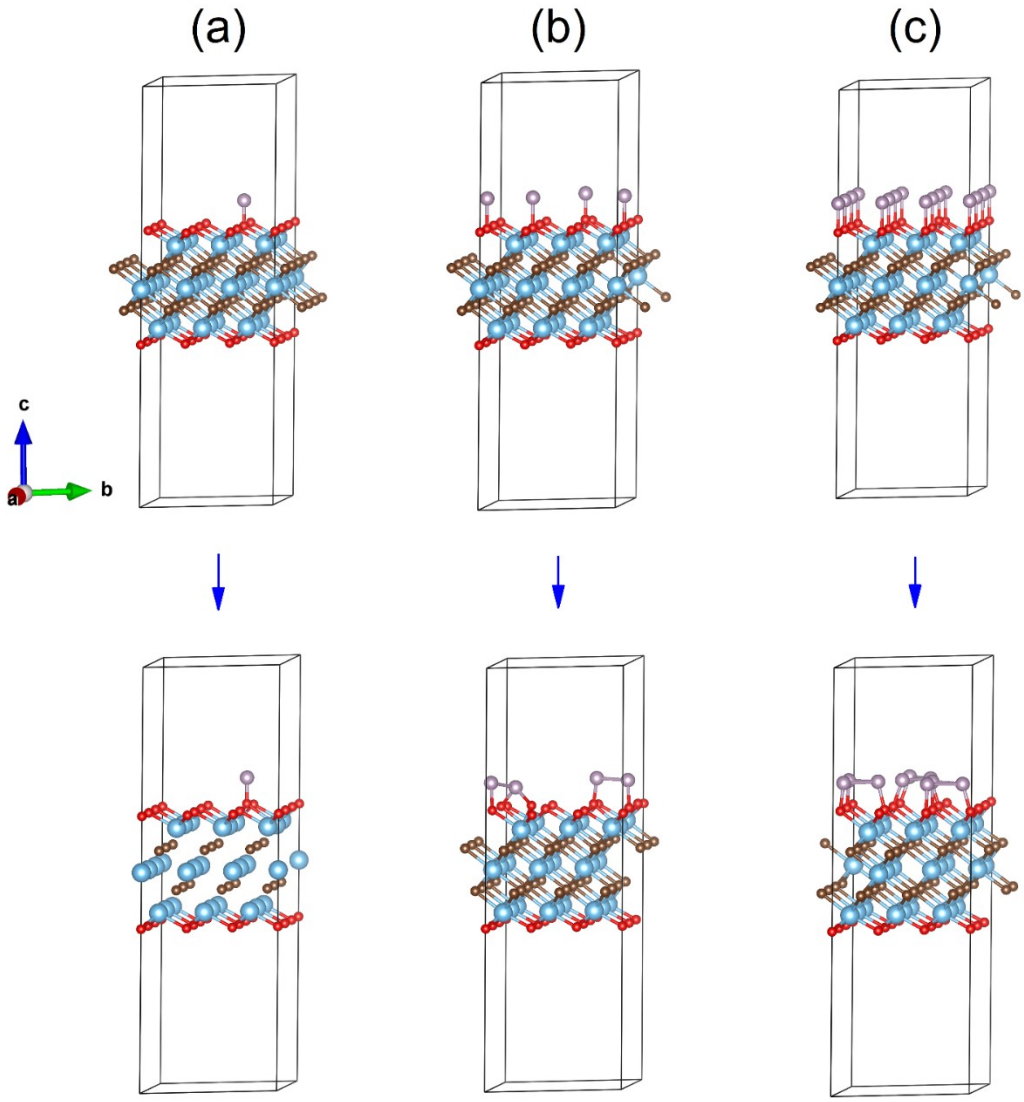

Figure S8. Before and after optimization of different P concentrations $Ti_3C_2O_2$-P system. (a) $Ti_3C_2O_2P_{0.11}$, (b) $Ti_3C_2O_2P_{0.33}$ and (c) $Ti_3C_2O_2P$. Ti, C, O, and P atoms are represented in blue, brown, red, and purple, respectively.

Whether the P atoms can be adsorbed on the $Ti_3C_2O_2$ Mxene surface with high concentration is further discussed from the calculation aspects. As shown in Figure S8, for the 3 × 3 supercell, a single P atom can stably be adsorbed on the surface of the $Ti_3C_2O_2$ monolayer. However, when the doping concentration is increased to 33%, the P atoms tended to form clusters with each other instead of being adsorbed on the surface of the $Ti_3C_2O_2$. This phenomenon is more obvious for the full coverage adsorption of P atoms.

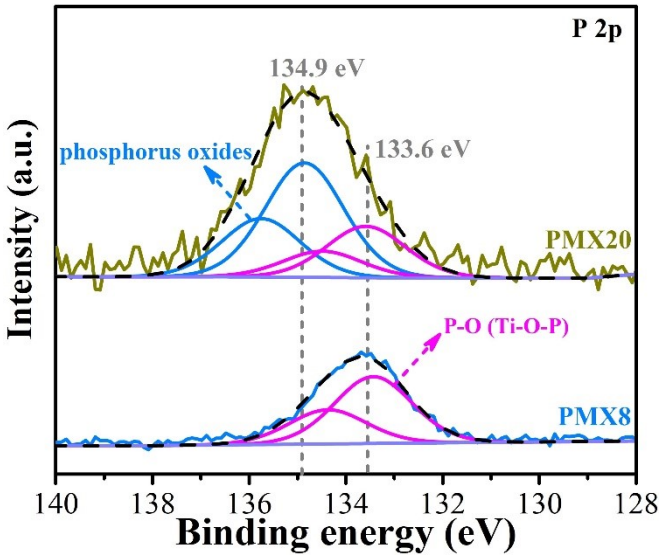

Figure S9 P2p XPS spectra of PMX8 and PMX20.

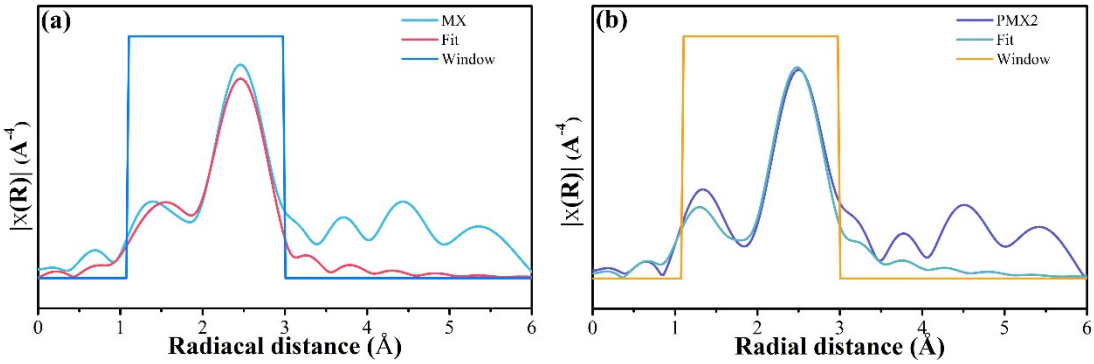

Figure S10 Ti K-edge EXAFS fitting results for (a) MX and (b) PMX2.

Table S1 Ti K-edge EXAFS fitting results. CN is the average coordination number, R is the distance from absorbed atom, and σ^2 the Debye–Waller factor. R-factor denotes a quality factor of the fitting, and ΔE_0 the energy shift from the absorption edge energy E_0.

Sample	Path	CN	△R, Å	R, Å	D-W factor(σ^2), Å^2	△E_0, eV	R-factor, %
MX	Ti-O/F	2.0(2)	0.09(2)	2.06(2)	0.004(2)	7.7	1.5
	Ti-C	4.2(6)	-0.01(1)	2.18(1)	0.009(2)	-6.5	
	Ti-Ti	7.8(4)	-0.04(2)	3.01(2)	0.009(1)	-9.2	

PMX2	Ti-O/F	1.8(2)	-0.02(2)	1.95(2)	0.003(1)	-4.9	1.2
	Ti-C	3.8(4)	0.01(1)	2.15(1)	0.003(1)	-9.7	
	Ti-Ti	5.9(2)	0.10(1)	3.03(1)	0.005(1)	-7.3	
	Ti-P	0.7(5)	0.09(3)	3.48(3)	0.012(3)	-6.9	

Table S2 Comparison of capacitive performance of PMX2 and other reported heteroatoms doped $Ti_3C_2T_X$ MXene.

Samples	Electrolyte	Specific capacitance	Cycling stability	References
PMX2	1 M H_2SO_4	437 F g^{-1} at 2 mV s^{-1} and 435 F g^{-1} at 1 A g^{-1}	94.3 % retention after 20000 cycles at 10 A g^{-1}	This work
N-$Ti_3C_2T_X$	1 M H_2SO_4	192 F g^{-1} at 1 mV s^{-1}	92 % retention after 10000 cycles at 50 mV/s	[7]
N, S-$Ti_3C_2T_X$	1 M H_2SO_4	340 F g^{-1} at 1 A g^{-1}	/	[8]
N-$Ti_3C_2T_X$	6 M KOH	190 F g^{-1} at 5 mV s^{-1}	/	[9]
V-$Ti_3C_2T_x$	2 M KCl	365.9 F g^{-1} at 10 mV/s	95 % retention after 5000 cycles at 10 A g^{-1}	[10]
Nb-$Ti_3C_2T_X$	6 M KOH	Maximum 442.7 F g^{-1}	70.5 % retention after 2000 cycles	[11]
P-$Ti_3C_2T_x$	1M H_2SO_4	320 F g^{-1} at 0.5 A g^{-1}	93.1 % retention after 5000 cycles at 5 A g^{-1}	[12]
N, S- $Ti_3C_2T_x$	1M Li_2SO_4	175 F g^{-1} at 2 mV s^{-1}	90.1 % retention after 5000 cycles at 2 A g^{-1}	[13]
N-$Ti_3C_2T_X$	3 M H_2SO_4	927 F g^{-1} at 5 mV s^{-1}	81.7 % retention after 20000 cycles at 10 A g^{-1}	[14]

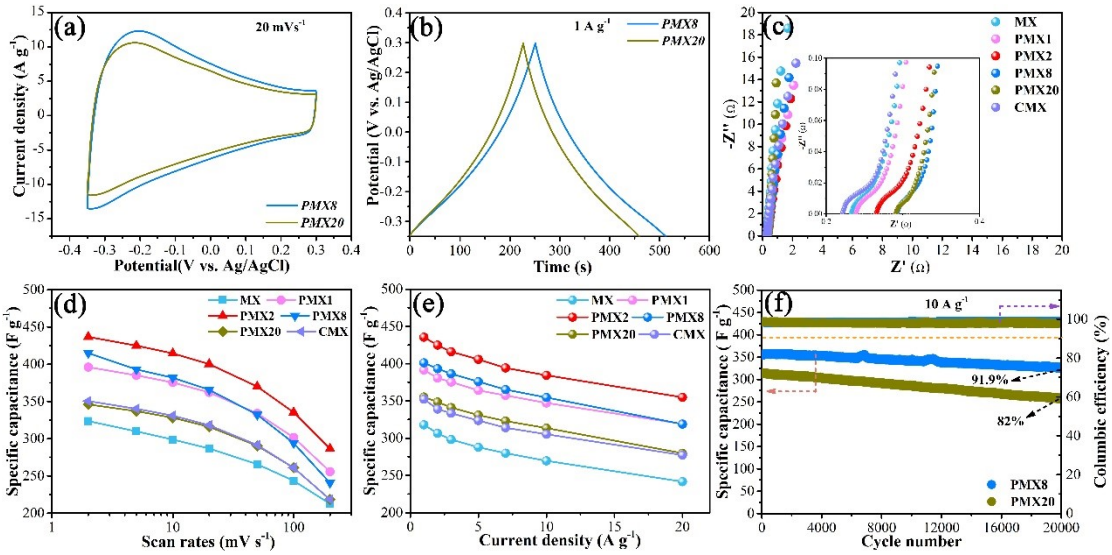

Figure S11 (a) CV curves of PMX8 and PMX20 at 20 mV s^{-1}, (b) GCD curves of the two samples at 1 A g^{-1}, (c) EIS plots of MX, PMX1, PMX2, PMX8, PMX20 and CMX, (d) capacitance vs. scan rates for the six samples, (e) gravimetric capacitance of the six samples at current densities from 2 to 20 A g^{-1}, (f) cyclic stability of PMX8 and PMX20 at 10 A g^{-1}.

Table S3 EIS fitting results for MX, PMX1, PMX2 and CMX.

	MX	PMX1	PMX2	CMX
R_s (Ω)	0.2398	0.2467	0.2726	0.2296
C_d (F)	0.0859	0.0851	0.0805	0.0476
R_{ct} (Ω)	0.0607	0.0548	0.0586	0.0539
CPE-T	0.7027	0.9435	1.028	0.8507
CPE-P	0.9601	0.9369	0.9279	0.9418

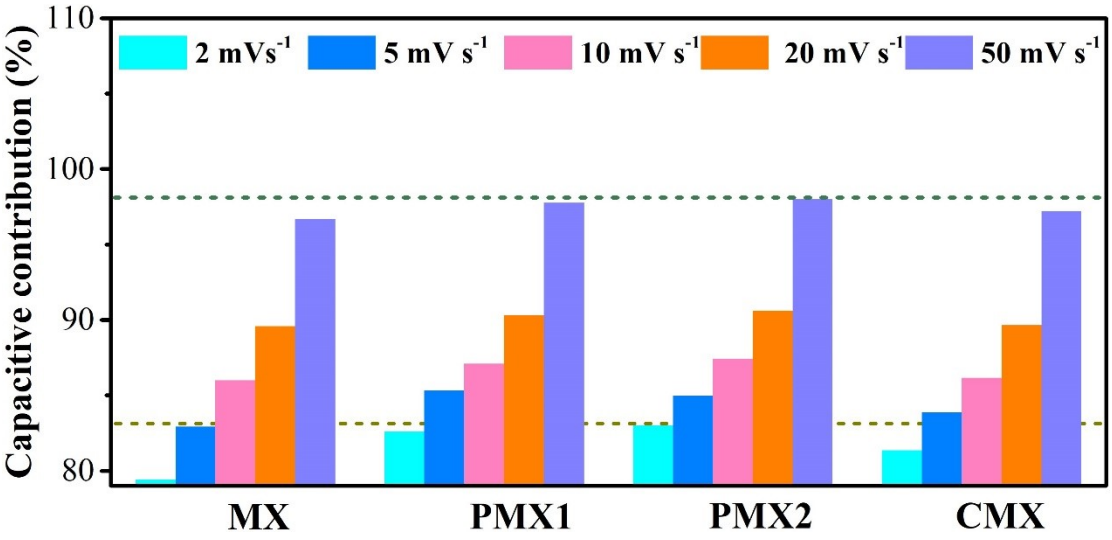

Figure S12 Capacitive contribution of MX, PMX1, PMX2 and CMX at scan rates from 2 to 50 mV s^{-1}.

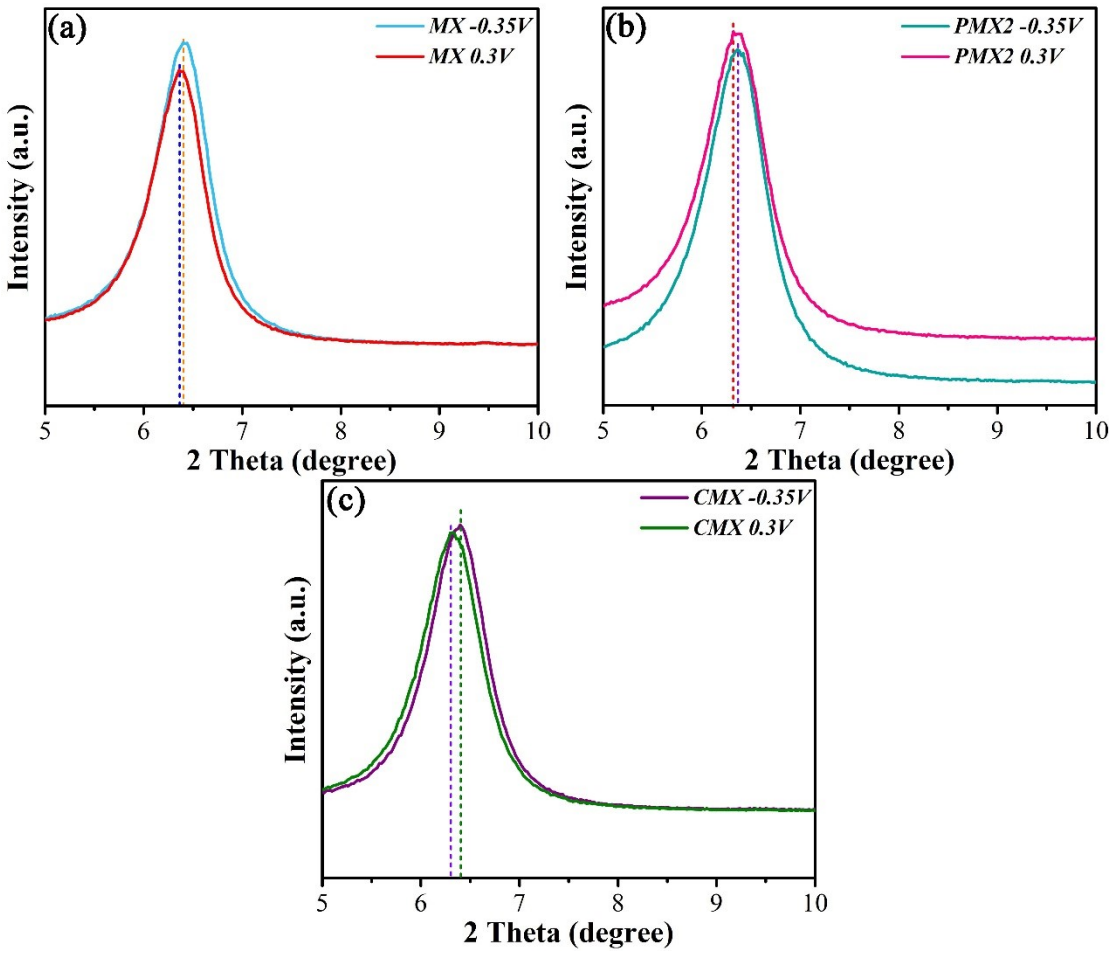

Figure S13 *Ex situ* XRD spectra of (a) MX, (b) PMX2 and (c) CMX.

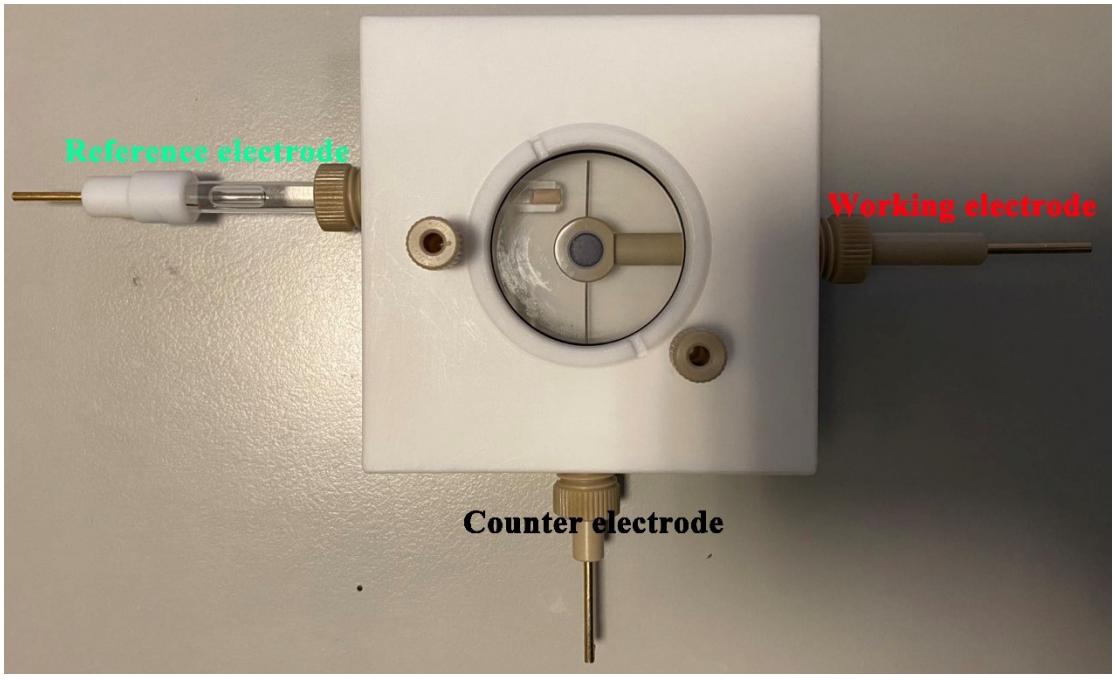

Figure S14 Photo for in-situ Raman device.

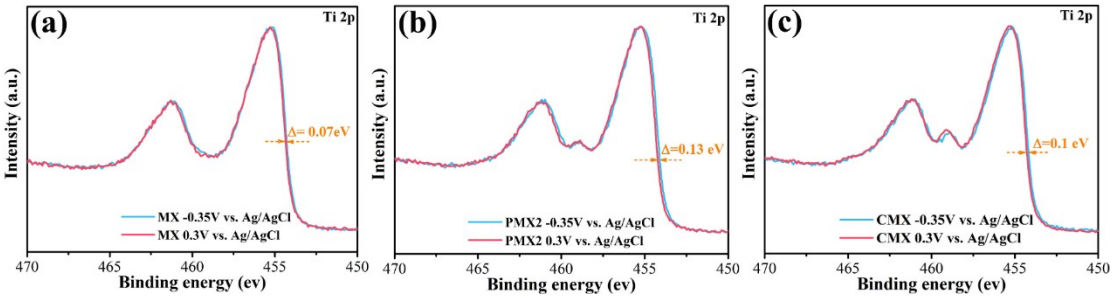

Figure S15 Ti 2p XPS spectra of (a) MX, (b) PMX2 and (c) CMX at potentials of -0.35 and 0.3 V vs. Ag/AgCl reference electrode.

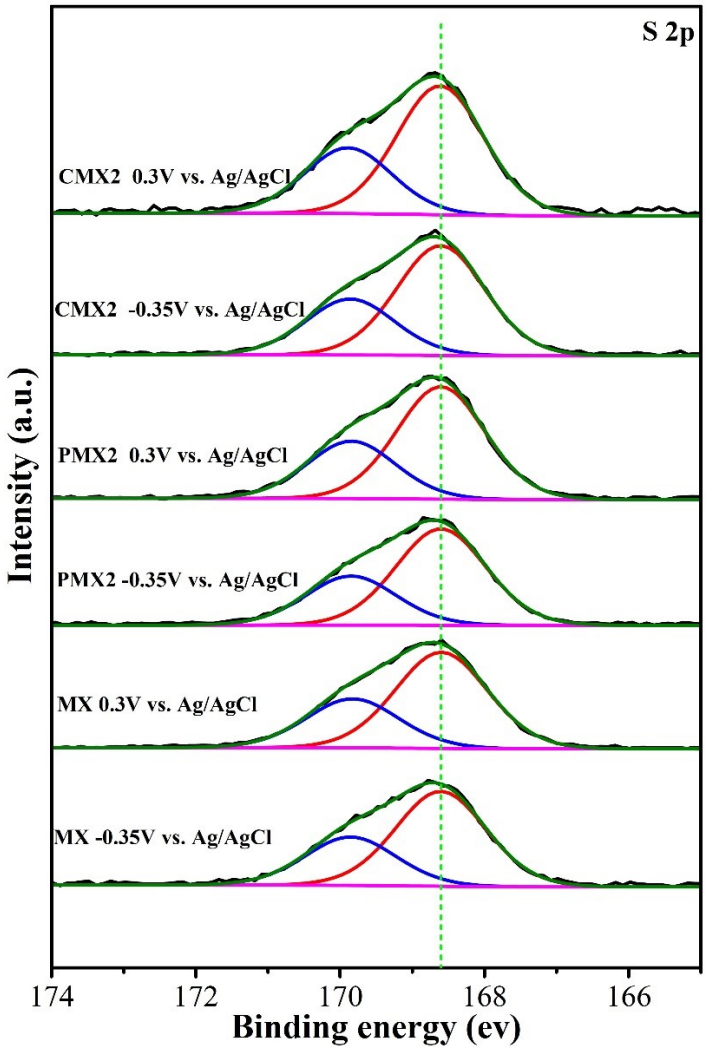

Figure S16 S 2p XPS spectrum for calibrating XPS results of MX, PMX2 and CMX.

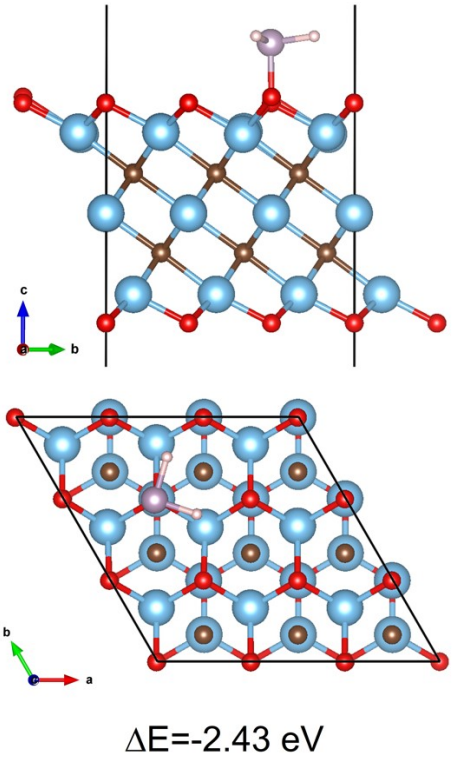

Figure S17 Top and side views of the hydrogen adopted in $Ti_3C_2O_2$-P system. Ti, C, O, H and P atoms are represented in blue, brown, red, flaxen and purple, respectively.

Based on Figure S16, the hydrogen atoms exhibit a strong binding effect with P atoms. Two H atoms can be adsorbed on one P atom stably with the binding energy of -2.43 eV, which is consistent with the fact that the five outermost electrons of the P element give it the ability to bond to multiple atoms.

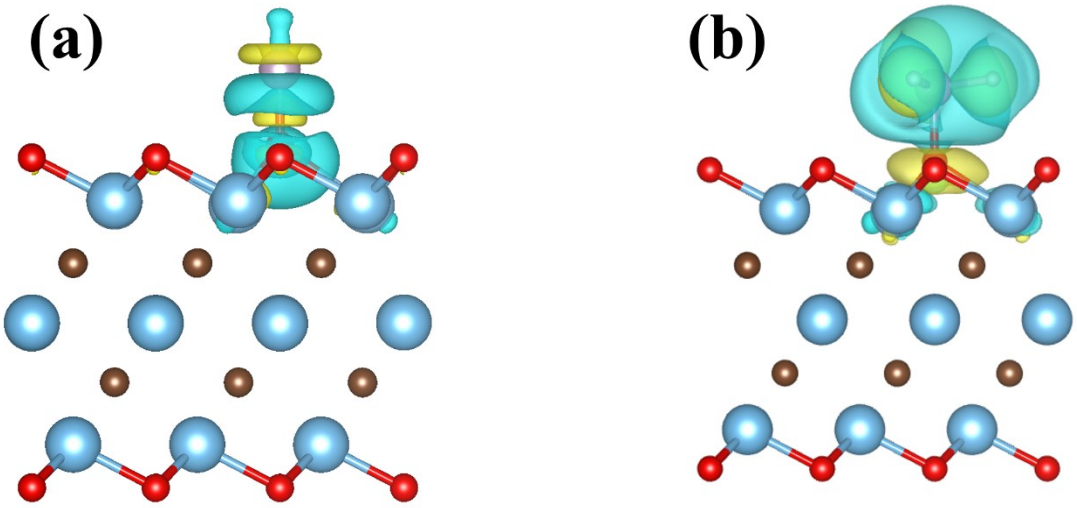

Figure S18 Differential charge density distributions of $Ti_3C_2O_2$-P before (a) and after (b) the surface P bonding with two protons. The yellow and blue-green regions indicate electron accumulation and depletion, respectively. Ti, C, O, H and P atoms are represented in blue, brown, red, flaxen and purple, respectively.

The differential charge density results (Figure S17a) show that the grafting of a phosphorus atom on surface oxygen atom of MXene leads to 0.91 electron loss for phosphorus and 1.85 electron loss for the titanium linked with oxygen and phosphorus. By comparison, when extra two protons bind with the surface grafted phosphorus atom, 1.48 electron and 1.88 electron losses are observed in phosphorus and the titanium linked with oxygen and phosphorus, respectively.

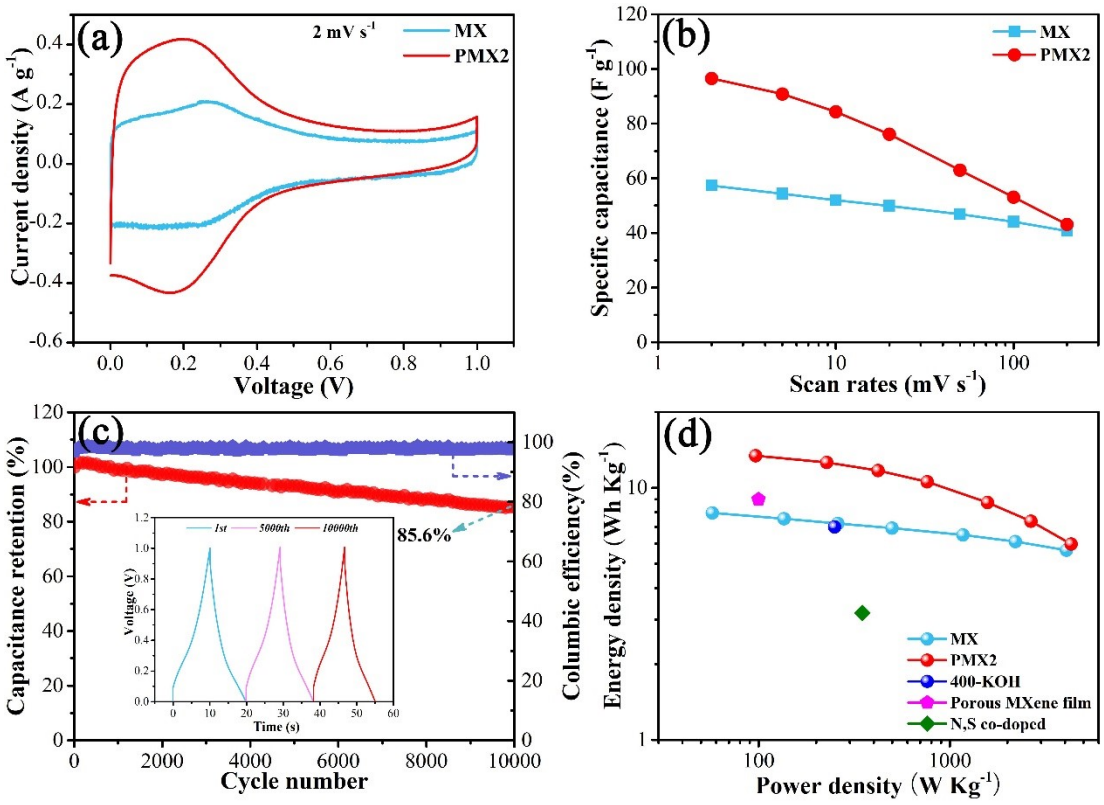

Figure S19 (a) CV curves of MX- and PMX2-based symmetric supercapacitors at 2 mV s^{-1}, (b) specific capacitance vs. scan rates for MX- and PMX2-based symmetric supercapacitors, (c) cyclic stability of PMX2-based supercapacitors at 5 A g^{-1}. Inset shows GCD curves at 1st, 5000th, and 10000th cycles, and (d) energy density vs. power density plot for MX- and PMX2-based symmetric supercapacitors.

References

1. G. Kresse and J. Furthmüller, *Physical review B*, 1996, **54**, 11169.
2. G. Kresse and D. Joubert, *Physical review b*, 1999, **59**, 1758.
3. J. P. Perdew, K. Burke and M. Ernzerhof, *Physical review letters*, 1996, **77**, 3865.
4. A. Jain, S. P. Ong, G. Hautier, W. Chen, W. D. Richards, S. Dacek, S. Cholia, D. Gunter, D. Skinner and G. Ceder, *APL materials*, 2013, **1**, 011002.
5. W. Tang, S. Chill and G. Henkelman, *Journal*, 1970.
6. K. Fan, Y. Ying, X. Luo and H. Huang, *Physical Chemistry Chemical Physics*, 2020, **22**, 16665-16671.
7. Y. Wen, T. E. Rufford, X. Chen, N. Li, M. Lyu, L. Dai and L. Wang, *Nano Energy*, 2017, **38**, 368-376.
8. L. Liao, D. Jiang, K. Zheng, M. Zhang and J. Liu, *Adv. Funct. Mater.*, 2021, **31**, 2103960.
9. C. Lu, L. Yang, B. Yan, L. Sun, P. Zhang, W. Zhang and Z. Sun, *Adv. Funct. Mater.*, 2020, **30**,

2000852.
10. Z. W. Gao, W. Zheng and L. Y. S. Lee, *Small*, 2019, **15**, 1902649.
11. M. Fatima, J. Fatheema, N. B. Monir, A. H. Siddique, B. Khan, A. Islam, D. Akinwande and S. Rizwan, *Front Chem*, 2020, **8**, 168.
12. Y. Wen, R. Li, J. Liu, Z. Wei, S. Li, L. Du, K. Zu, Z. Li, Y. Pan and H. Hu, *J. Colloid Interface Sci.*, 2021, **604**, 239-247.
13. C. Yang, W. Que, Y. Tang, Y. Tian and X. Yin, *J. Electrochem. Soc.*, 2017, **164**, A1939-A1945.
14. C. Yang, Y. Tang, Y. Tian, Y. Luo, M. Faraz Ud Din, X. Yin and W. Que, *Adv. Energy Mater.*, 2018, **8**.